PNAS RESEARCH ARTICLE | APPLIED PHYSICAL SCIENCES

Command of three-dimensional solitary waves via photopatterning

Chao-Yi Li[a,b,1], Xing-Zhou Tang[c,1], Xiao Yu[a], Noe Atzin[c], Zhen-Peng Song[b], Chu-Qiao Chen[c], Nicholas L. Abbott[d], Bing-Xiang Li[a,b,2], Juan J. de Pablo[c,e,2], and Yan-Qing Lu[a,2]

Affiliations are included on p. 9.

Edited by Noel Clark, University of Colorado Boulder, Boulder, CO; received March 12, 2024; accepted July 15, 2024

Multidimensional solitons are prevalent in numerous research fields. In orientationally ordered soft matter system, three-dimensional director solitons exemplify the localized distortion of molecular orientation. However, their precise manipulation remains challenging due to unpredictable and uncontrolled generation. Here, we utilize preimposed programmable photopatterning in nematics to control the kinetics of director solitons. This enables both unidirectional and bidirectional generation at specific locations and times, confinement within micron-scaled patterns of diverse shapes, and directed propagation along predefined trajectories. A focused dynamical model provides insight into the origins of these solitons and aligns closely with experimental observations, underscoring the pivotal role of anchoring conditions in soliton manipulation. Our findings pave the way for diverse fundamental research avenues and promising applications, including microcargo transportation and optical information processing.

three-dimensional soliton | liquid crystal | photopatterning | topological structure

Significance

Solitons, localized wave packets that exhibit particle-like behavior, are ubiquitous in physical and biological sciences. However, stable multidimensional dynamic solitary waves and their manipulation remain experimentally elusive until very recently. We now show that three-dimensional dissipative solitons can nucleate at any desired location in orientationally ordered system. Manipulation of soliton generation area, combined with directed propagation and confinement of solitons, promise potential applications in microcargo transportation and optical information processing. Understanding how flexoelectricity and anchoring conditions contribute to the generation and manipulation of solitons is essential to advancing these technologies.

Solitary waves, often termed "solitons," are localized wave packets that propagate with minimal changes in shape or dissipation at a constant speed (1, 2). These waves can manifest at macroscopic scales, evident in cosmic phenomena (3), or on a microscopic scale, such as particle-like excitations that exhibit bound states akin to molecules (4). This distinctive wave propagation mode is pivotal in various events, from pulse propagation in biological systems (5, 6) to dissipative light bullets in optical applications (7, 8).

Drawing inspiration from solitary waves in nature, researchers have delved into the intriguing behaviors of multidimensional solitons in liquid crystals (LCs). The optical anisotropy of LCs, which arises from the orientational order of LC molecules, offers a platform for generating and propagating optical solitons, called nematicons (9, 10). Within chiral nematic LCs (NLCs), particle-like topological director solitons such as skyrmions (11), torons (12), and hopfions (13) have been identified. Martinez et al. utilized photo-responsive layers in contact with solitons to demonstrate potential uses of light-soft matter interaction for light-driven micromachines (14). In NLCs, solitons, which reflect localized distortions of the director indicating the average molecular orientation, can emerge under certain magnetic (15) and electric fields (16, 17). Li et al. (18) detailed the electrically driven three-dimensional (3D) director solitons that maintain confined shapes and endure collisions in the (–, –) type of NLC, wherein both $\Delta\varepsilon$ and $\Delta\sigma$ are negative. These director solitons are termed "director bullets" or "directrons," akin to "optical bullets" for the 3D optical solitons. Directrons can be redirected along curved trajectories by modulating the electric field in the ionic-salt-doped NLC (19). Aya et al. (20) showcased the varied kinetics of directrons and their self-assembly into lattice ordering via electric field alteration in the (–, +) type NLC. Das et al. (21, 22) elucidated how anchoring, surface strain, and abrupt changes in nematic orientations can dictate directron paths. Subsequently, the dynamics of dissipative directrons have been analyzed by manipulating the electric field across material systems including (+, +) nematics (23), chiral-nematics (24), and smectics (25). Several simulation works have corroborated with experiments (26–28), suggesting flexoelectricity as the primary influence in the genesis and movement of directrons (18, 26, 29). Research indicates that directrons invariably originate from unforeseen locations at irregularities present in a uniform alignment background, achievable by methods such as rubbing (18, 30) and photopatterning (24, 31–33). However, there is no report on the precise generation of such dissipative directrons at specific locations and times or confinement of them within arbitrary micron-scaled patterns.

In this work, we effectively manipulate 3D directrons in orientationally ordered environments consisting of programmable patterns prepared by lithography systems with different ultraviolet (UV) light. We precisely orchestrate the generation of these solitons at designated spatial locations, ensuring accuracy in both their origin and direction. Further, we achieve localization in

Author contributions: B.-X.L., J.J.d.P., and Y.-Q.L. designed research; C.-Y.L. and X.-Z.T. performed research; C.-Y.L., X.-Z.T., X.Y., N.A., Z.-P.S., and C.-Q.C. analyzed data; and N.L.A., B.-X.L., J.J.d.P., and Y.-Q.L. wrote the paper.

The authors declare no competing interest.

This article is a PNAS Direct Submission.

[1]C.-Y.L. and X.-Z.T. contributed equally to this work.

[2]To whom correspondence may be addressed. Email: bxli@njupt.edu.cn, depablo@uchicago.edu, or yqlu@nju.edu.cn.

This article contains supporting information online at https://www.pnas.org/lookup/suppl/doi:10.1073/pnas.2405168121/-/DCSupplemental.

Published August 28, 2024.

areas characterized by low anchoring energy W. Our simulations highlight variations in anchoring energy across regions. These low-anchoring areas are critical for the initiation of directrons at specific regions. A strong correlation between our experimental findings and simulation outcomes validates the efficacy of the photopatterning combined with multilight-source techniques to produce orientationally ordered soft material systems for the generation and manipulation of solitary waves and suggests potential applications in microcargo transportation and optical information processing (18, 19).

Results

Pattern Design and Fabrication. To guide the LC orientations, we utilize photoalignment techniques on patterned surfaces. First, we coat the glass substrates with a UV-polarization-sensitive azobenzene dye SD1. We then align it using linearly polarized UV light. Upon UV exposure at a designated wavelength, λ = 405 nm, SD1 aligns itself perpendicular to the light's polarization, creating a consistent background (Fig. 1*A*). To introduce predetermined patterns to SD1, we apply the photoalignment method with a digital-micro-mirror-device microlithography system (Fig. 1*B* and *SI Appendix*, *Text* and Fig. S1) and expose SD1 to UV light at another distinct wavelength, λ = 365 nm. These predetermined patterns, generated by light at a wavelength of 365 nm, are superimposed on the orientational background created by light at 405 nm. Next, we introduce 4′-butyl-4-heptyl-bicyclohexyl-4-carbonitrile (CCN-47) into the NLC cells, which have a defined thickness of d = 8.0 ± 0.3 μm. Notably, CCN-47 is an NLC with negative anisotropies for both permittivity and electric conductivity, conducive to directron generation (18, 26, 29). The anchoring of the SD1 film ensures the NLC aligns with our intended patterns. We then apply a sinusoidal AC electric field $E = (0, 0, Esin(2\pi ft))$ perpendicular to the nematic slab. Meanwhile, the voltage related to this field is defined as $U = Ed$. Since the electric field is along z-axis, the voltage can be represented as $U = Esin(2\pi ft)d$, where d is considered as the thickness of the sample. This field, adjustable within a frequency f range from 500 Hz to 1 kHz, initiates the emergence and movement of directrons (Fig. 1*C* and *SI Appendix*, Fig. S2).

Realization of Directron Source. Surface patterns on a uniform substrate are crafted as detailed earlier. Our experiments show that directrons consistently emanate from a particular region, reminiscent of a machine gun's rapid-fire action. We have dubbed this structure

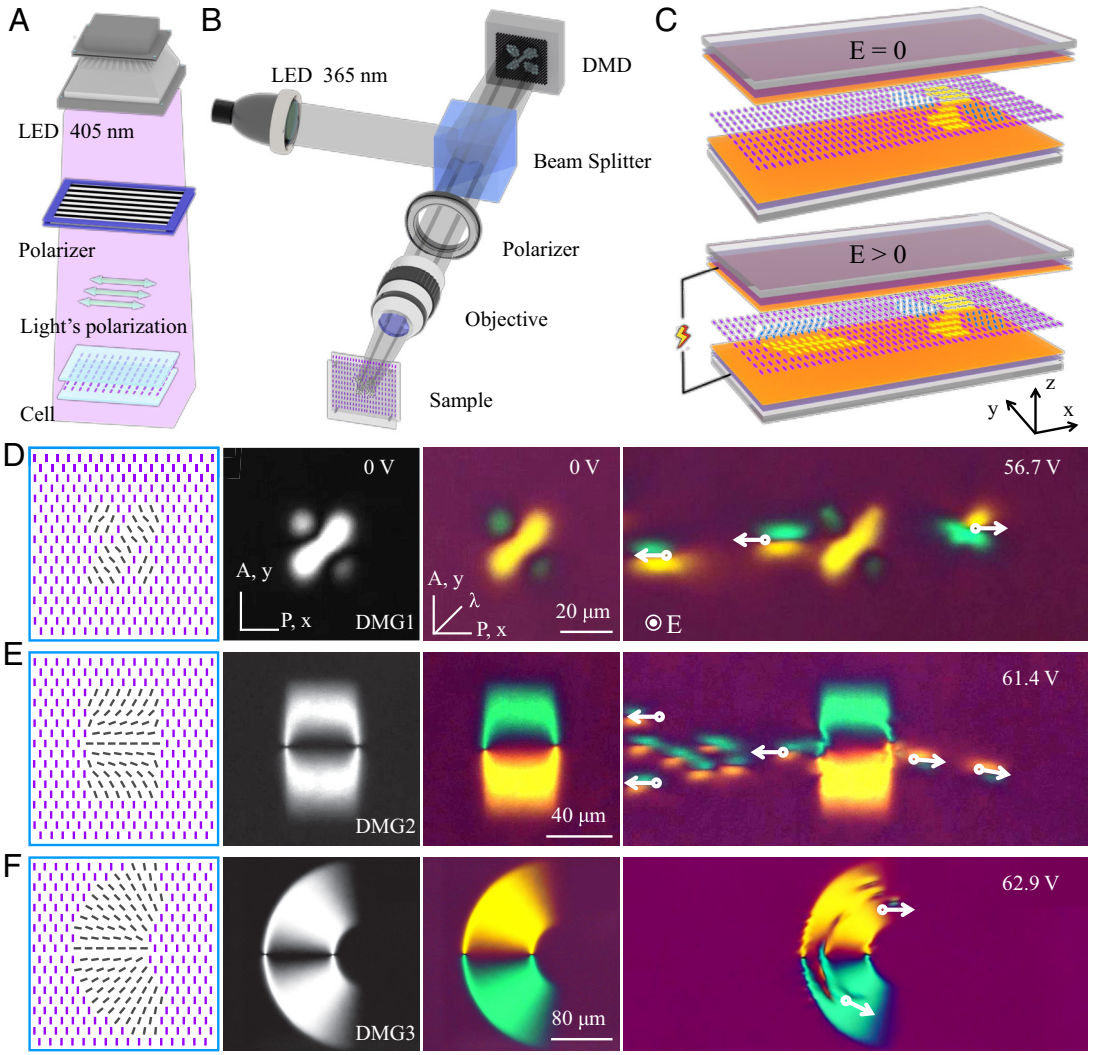

Fig. 1. Programmable and prelocated sources of directrons. (*A*) Set up a homogeneous background using SD1. (*B*) Craft the desired pattern utilizing the photoalignment technique based on a digital-micro-mirror device. (*C*) Illustration of directrons' generation by applying an AC field onto an NLC cell. (*D*) Directron Machine Gun 1 (DMG1): A quadripartite symmetric butterfly structure, f = 550 Hz. (*E*) DMG2: Features a pair of +1/2 and −1/2 defects, f = 650 Hz. (*F*) DMG3: Adopts a toroidal pattern, f = 681 Hz. Three DMGs are presented with the director configuration and the images taken under crossed polarizers with and without a full waveplate λ = 530 nm.

that serves as the source of directrons (director bullets) the "Directron Machine Gun" (DMG). The varied sources illustrated in Fig. 1 *D*–*F* are labeled DMG1-3. DMG1 represents a quadripartite symmetric butterfly structure, DMG2 features a pair of +1/2 and −1/2 defects, and DMG3 displays a toroidal configuration. All DMGs prove proficient in generating directrons, demonstrating that patterns created by light at a wavelength of 365 nm, superimposed on the orientational background generated by 405 nm light, are effective directron sources regardless of whether they contain defects (Movies S1–S3). Note that the generated directrons are (2+1+1)D solitons (18) with 3D deformation of the director in orientationally ordered environments, where "2" refers to the self-confinement along the x and y axes; the first "1" represents the transversal confinement along the z-axis imposed by surface anchoring; the second 1 specifies the unidirectional propagation of directrons (18). To further check the dimensionalities of solitons, we performed a Derrick-Hobart rescaling analysis (*SI Appendix, Text*) and demonstrated that there is no stable 3D solution. Further rescaling analysis can similarly be performed using the specific free energy expression with all actual terms in Eq. **1**. The reference 3D for soliton in this work is only in terms of deformation of director. The design motivation for DMG1 and DMG5 is to imitate the circular director deformation created by particles in a homogeneous background. To further control the precise location of soliton generation, we introduced singular defect lines into the patterns of DMG2 and DMG3 to simulate irregularities. DMG4 and DMG6 extend from circular to radial distortion patterns. A comprehensive examination of the DMG4-6 patterns is available in *SI Appendix*, Fig. S3. Since patterns with diverse distortions can generate solitons, we then designed patterns with uniform alignment to purposely investigate and confirm the mechanisms behind soliton generation.

Electrical Control of DMGs. To investigate the impact of electric condition on DMGs with different domain sizes and shapes of the inner pattern, we establish an orientation difference of α = 91° between the inner pattern ($\hat{\mathbf{n}}^*$) and the background ($\hat{\mathbf{n}}_0$). This deviation from 90° introduces a tilt into our system. Such design ensures that the directors at the interface between inner and outer domains of the circles deviate toward the same direction, unlike the configuration with α = 90°, refer to *SI Appendix*, Fig. S4.

We contrast a circular domain by varying the size with three distinct diameters: 150 μm, 75 μm, and 20 μm. With a constant frequency of f = 500 Hz, varied voltages U, yield different observable phenomena. As shown in Fig. 2*A*, directrons initially manifest solely within the circular pattern at U = 46.6 V; elevating U incrementally instigates a transition in the director field within the circular domain to a more disordered state; Upon reaching 51.2 V, the directrons escape from the confining domain and travel freely to the surrounding uniform media (Movie S4). Fig. 2*B* elaborates on the electric conditions corresponding to different sizes, and the threshold voltage doesn't depend on the size of the pattern when the orientation difference is 91°. The black line signifies the threshold for generating directrons within the pattern, while the red line corresponds to the threshold for the chaotic phase. The area between the red and blue lines represents the chaotic phase. Beyond the blue line, the DMGs initiate the directrons. The figure reveals a linear relationship between U and f. The slope denoting directron triggering exceeds the other two cases, indicating that the system faces more resistance emitting directrons into the background at elevated frequencies.

The Fig. 2*C* illustrates the variances in directron behavior across different shapes under varying U. We evaluate the triangle (three edges), the polygon (eight edges), and the circle (analogous to infinite edges). The observed results show a minute difference with those in Fig. 2*A*, with the accompanying image on the right highlighting scenarios where the voltage is just around the threshold for the directrons to escape from the confined region (Movie S5). Fig. 2*D* provides insights into the electric conditions across diverse frequencies for different shapes, showing that the threshold voltage does not depend on the shape of the pattern when the orientation difference is 91°. The black line signifies the threshold for generating directrons within the pattern, while the red line corresponds to the threshold for the chaotic phase.

We observed that DMGs exhibit distinct behaviors under varied electrical scenarios. Directrons are more readily generated within internal patterns and the director field turns chaotic phase as U increases. DMGs catalyze directron activity at voltages surpassing the stipulated threshold. This intriguing phenomenon may arise due to the anchoring energy disparity between areas exposed to UV light of differing wavelengths. We determine the anchoring energy of CCN-47 at 55 °C and the anchoring energy ratio for these two light sources stands at $\frac{W_{365}}{W_{405}} = 0.66 \pm 0.19$, where the subscripts "365" and "405" denote the light wavelengths (*Materials and Methods* and *SI Appendix*, Fig. S5). The ratio of threshold voltages required to generate directrons is $\frac{U_{365}}{U_{405}} \approx 0.90$. In addition, the applied electric field energy is proportional to the square of voltage value so that the ratio of applied energy is $\frac{W^E_{365}}{W^E_{405}} \approx 0.81$, within the range of 0.66 ± 0.19. This result is consistent with our hypothesis that differences in anchoring energy can lead to different threshold voltages for soliton generation.

The Fig. 2*E* displays simulation results across varying voltages and diameters. In this figure, U_0 represents the voltage at which DMGs emit directrons into the background. Fig. 2*F* illustrates simulation outcomes associated with different shapes, corresponding to the details in Fig. 2*C*. Notably, these simulation results align with these observations across different voltages and the director distributions refer to *SI Appendix*, Fig. S6.

In summary, the generation and emission thresholds of solitons for patterns with the same orientation are dependent on the voltage but not size and shape. In the next section, we use uniform patterns with different α to investigate the effect of orientation variance on soliton emission.

Effect of Orientation Variance between Areas. To study the relationship between the orientation variance and the voltage applied on DMGs for generation of directrons, we established four circular DMGs: R1, R2, R3, and R4 (Fig. 3). The orientation difference ($\boldsymbol{\alpha}_i$) between the inner director field $\hat{\mathbf{n}}_i$ and the background director field $\hat{\mathbf{n}}_0$ stands at 45°, 60°, 75°, and 90° for these DMGs, respectively (Fig. 3 *A* and *B*). When subjected to varying electric conditions, these DMGs exhibit distinct behaviors. The threshold voltage U_{em} for directron emission varies. Fig. 3*C* illustrates that U_{em} for DMGs R1 through R4 are 52.5 V, 52.2 V, 51.9 V, and 51.6 V, respectively, with the AC field frequency is set to be constant at f = 500 Hz (Movie S6).

As the orientation difference $\boldsymbol{\alpha}_i$ increases, the required U_{em} decreases. This trend is also captured in our simulation results (Fig. 3*F* and *SI Appendix*, Fig. S7), where U_0 represents the voltage at which all DMGs emit directrons into the background. A DMG with a greater $\boldsymbol{\alpha}_i$ value consumes more elastic energy. Consequently, less elastic energy is available to counteract the generation of solitons, which compromises the stability of the structure. In Fig. 3*D*, we delineate the electric conditions initiating directron emission at various $\boldsymbol{\alpha}_i$ levels. A clear linear relationship exists between voltage and frequency; a larger $\boldsymbol{\alpha}_i$ demands a decreased U_{em} at a constant frequency to trigger directrons. As depicted in Fig. 3*E*, the

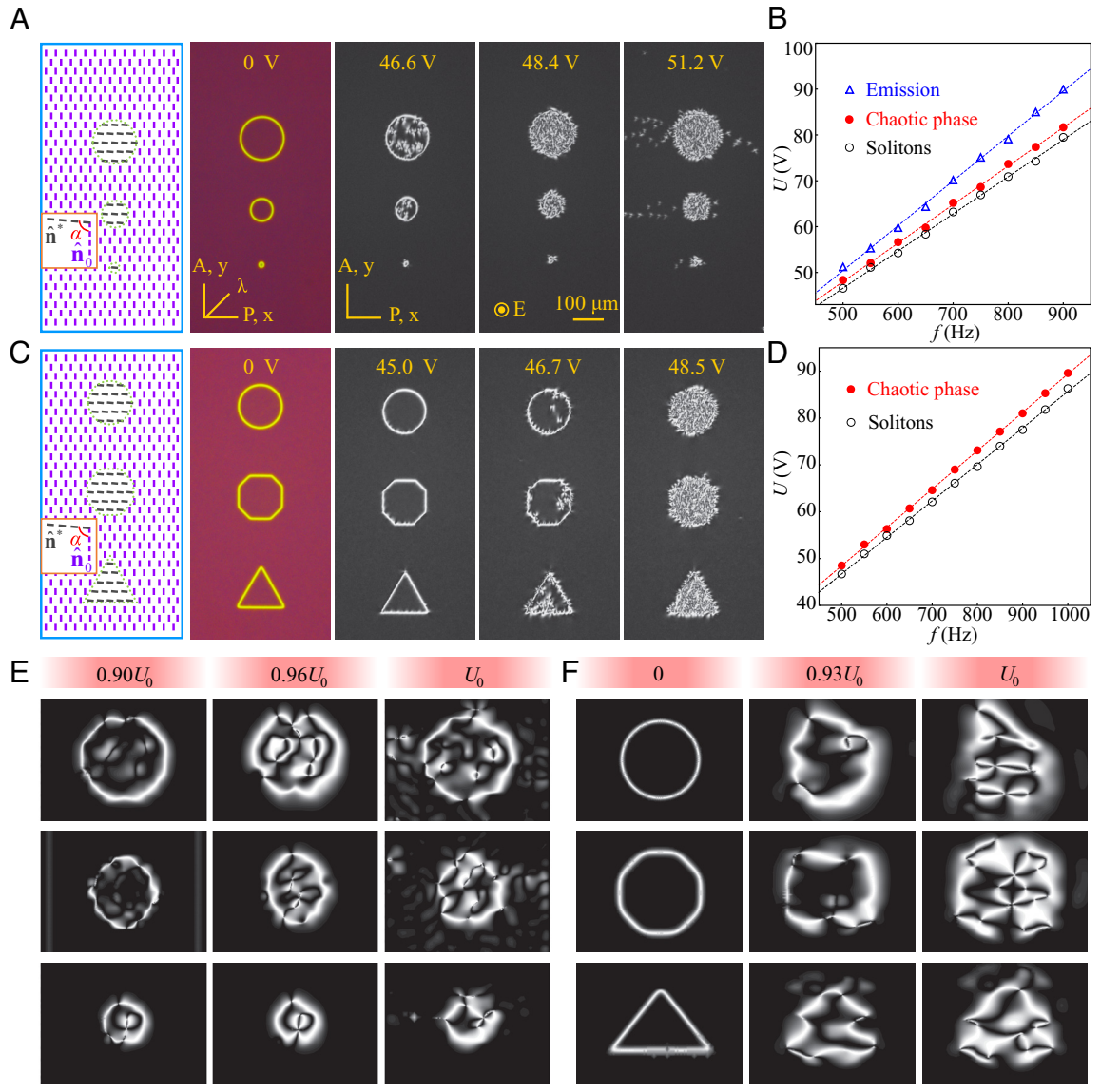

Fig. 2. Electrical controlled localization and emission of directrons in patterns with different UV exposure. (*A*) Director fields and polarizing optical representations for DMGs of varying diameters. (*B*) Electric conditions corresponding to the states of directrons within the pattern, chaotic states, and the emission of directrons into the background for DMGs of different sizes. (*C*) Director fields and polarizing optical diagrams for DMGs with diverse shapes. (*D*) Electric conditions pertaining to directrons located within the pattern and chaotic states on the verge of releasing directrons into the background for DMGs of varying shapes. (*E* and *F*) Simulation results aligned with the experiment. The dashed lines in *B* and *D* show the linear fitting.

increase of voltage or α_i results in the generation of more directrons within a set timeframe.

Directron Generation in Patterns of Varied Diameters and Orientations. In this section, we delve deeper into the influence of orientation variance and pattern size on the generating of directrons. We adjust the orientation to 45°, 60°, 75°, and 90° while varying the diameters at 22 μm, 33 μm, and 52 μm. Fig. 4 *A*–*C* displays their experimental representations. As with prior sections, the inner and outer patterns were illuminated with 365 nm and 405 nm respectively, during the photoalignment process. Fig. 4 *D* and *E* presents the voltages that produce directrons across varying sizes and orientations, in experiment and in simulation respectively. Here, *U* stands for the threshold voltage required for emitting directrons into the background and U_0 represents the threshold voltage for DMG, $\alpha_4 = 90°$.

Both the experimental and simulation outcomes underscore a consistent trend: DMGs generate directrons more efficiently when subjected to greater voltages, larger diameters, or pronounced orientation disparities. Concurrently, the impact of orientation diminishes as the inner pattern's size increases. Our simulations elucidate this behavior. A larger orientation mismatch or increased size requires more energy to be consumed to distort the director fields from the equilibrium state subscribed by the surface anchoring. Consequently, less elastic energy is available to counteract directron generation. In the simulation, we noticed that there is an intersection between the inner pattern and the background. Adjacent to this interface, both sections are initially homogeneous. Specifically, this particular region contributes additional elastic energy, susceptible to changes from both orientation and diameter. A larger diameter reduces the area ratio between this intersection and the inner pattern, explaining why orientation exerts a reduced influence with increased diameters.

Unidirectional Generation of Directrons. In this section, we explore the influence of the transition area on the generation of directrons, particularly how it can be used to dictate the progression direction of these directrons. We constructed a

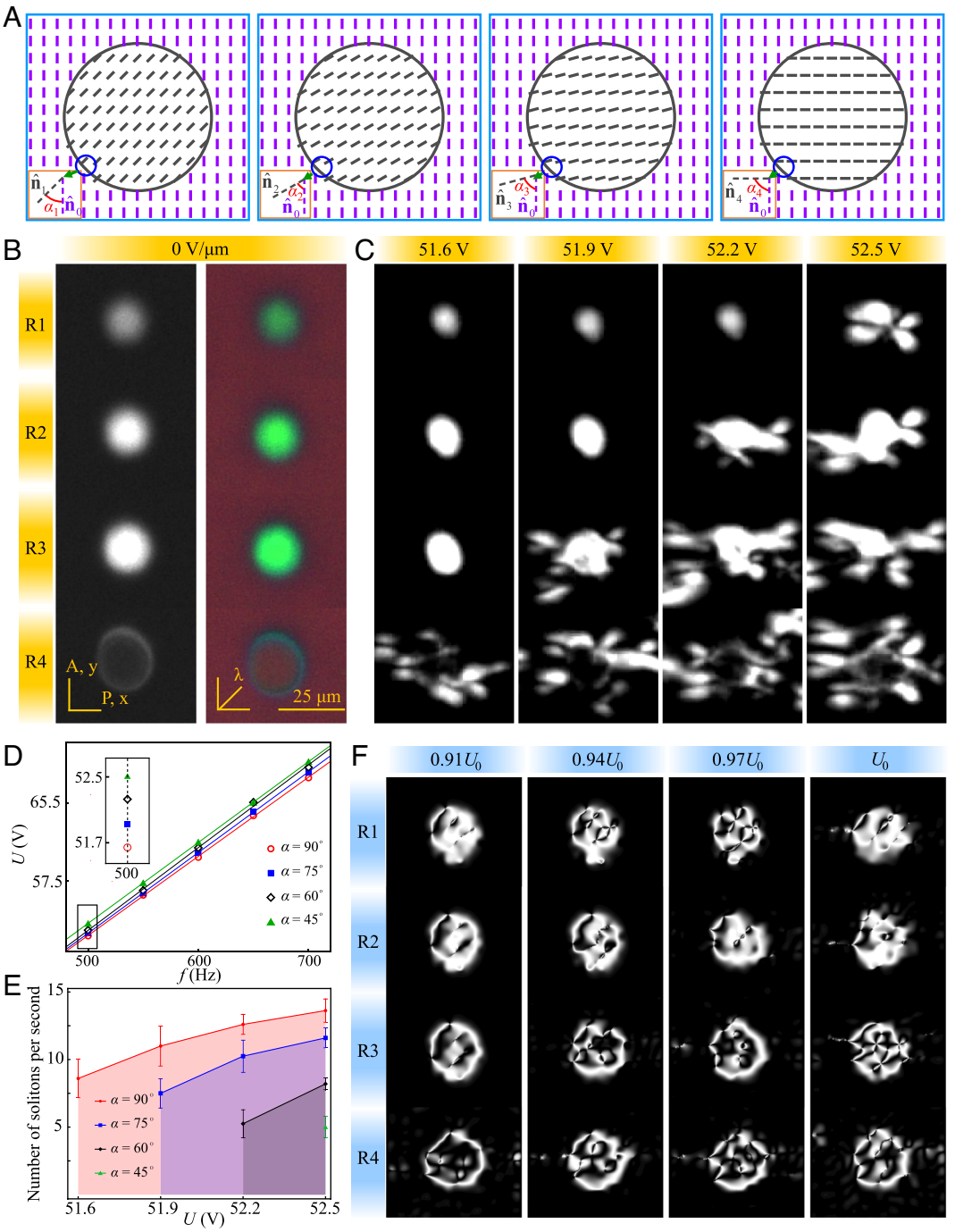

Fig. 3. Directron emission influenced by orientational and electrical differences. (*A*) Circular DMGs R1, R2, R3, and R4 characterized by orientation differences of 45°, 60°, 75°, and 90°, respectively. (*B*) Polarizing optical microscope (POM) figures captured at the absence of electric fields; displayed both with and without the full waveplate. (*C*) Phenomenon under diverse voltages. (*D*) Electric parameters required for the release of directrons into the background for each DMG. (*E*) Number of directrons generated from various DMGs over 1 s. (*F*) Simulation outcomes corresponding to the experiments.

rectangular domain, as illustrated in Fig. 5 *A* and *B*, where the orientation difference between the inner pattern ($\hat{\mathbf{n}}^*$) and the background ($\hat{\mathbf{n}}_0$) is set at $\alpha = 91°$. The right edge features a thick transition area exceeding 90 μm in length, resulting in a gradual shift in the director field. Conversely, on the remaining edges, the director field transitions abruptly with a thickness less than 15 μm.

Upon gradually increasing the applied voltage at $f = 900$ Hz, we initially detected directrons forming within a rectangular domain (Fig. 5*C*). This state subsequently evolved into a chaotic configuration (Fig. 5*D*) before the directrons eventually permeated into the surrounding background (Fig. 5*E*). Importantly, it is noted that the directrons have a higher tendency to progress outward from the interface, attributable to its smoother variation of director field. Building upon our earlier discussion, the interface consumes more elastic energy, resulting in an area that is less stable compared to other edges. This gradual transition in the director field provides a pathway that promotes the generation and migration of directrons. As a result, the design and width modulation of the interface enables the precise direction of directron emission. Fig. 5*F* delineates the electric conditions corresponding to the states depicted in Fig. 5 *C*–*F*, with the electric field-frequency relationship mirroring those in Figs. 2

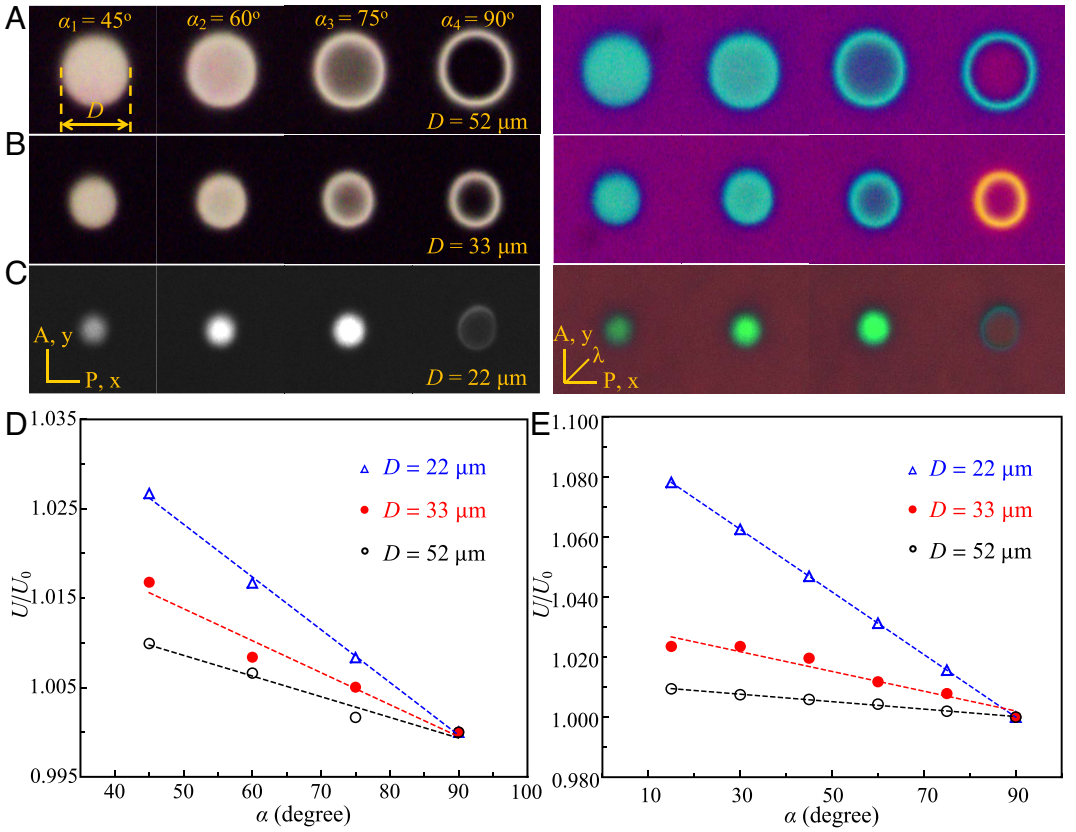

Fig. 4. Phase diagram of different diameters and orientations. (*A*–*C*) POM figures presented both with and without a full waveplate (530 nm) across distinct diameters. (*D*) Threshold voltage ratio required for emitting directrons into the background, varying by size and internal orientation in experiment, f = 600 Hz. (*E*) Threshold voltage ratio for different sizes and orientation in simulation.

and 3. The accompanying simulation in Fig. 5*G* validates our ability to manage the emission direction by controlling the asymmetry of the interface (Movie S7).

Localization of Directrons. Inspired by our previous research, we have the capability not only to initiate directrons from specific patterns but also to populate these patterns with directrons. Fig. 6

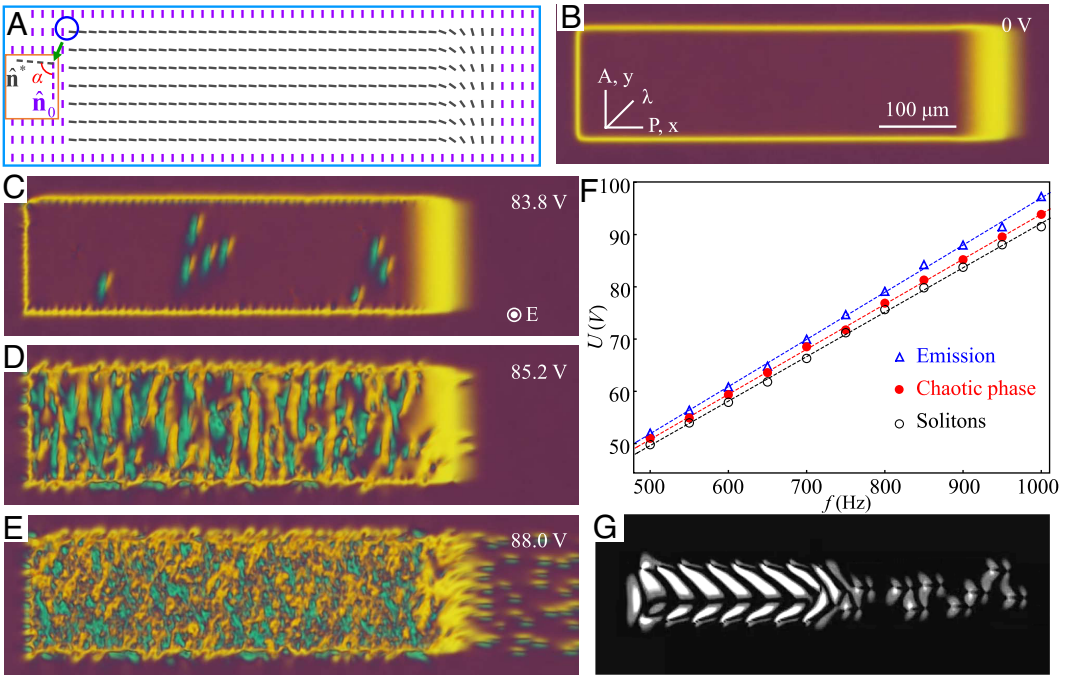

Fig. 5. Unidirectional generation of directrons by photopatterning. (*A*) Director field of a rectangular domain featuring an expanded intersection on the *Right*. (*B*) POM figures in the absence of an electric field. (*C*) Generation and (*D*) saturation of directrons within the rectangular domain. (*E*) Directrons emitting from the rectangular pattern via the intersection. (*F*) Electrical conditions corresponding to the states described in *C*–*E*. (*G*) Simulation results indicating directron emission from the intersection.

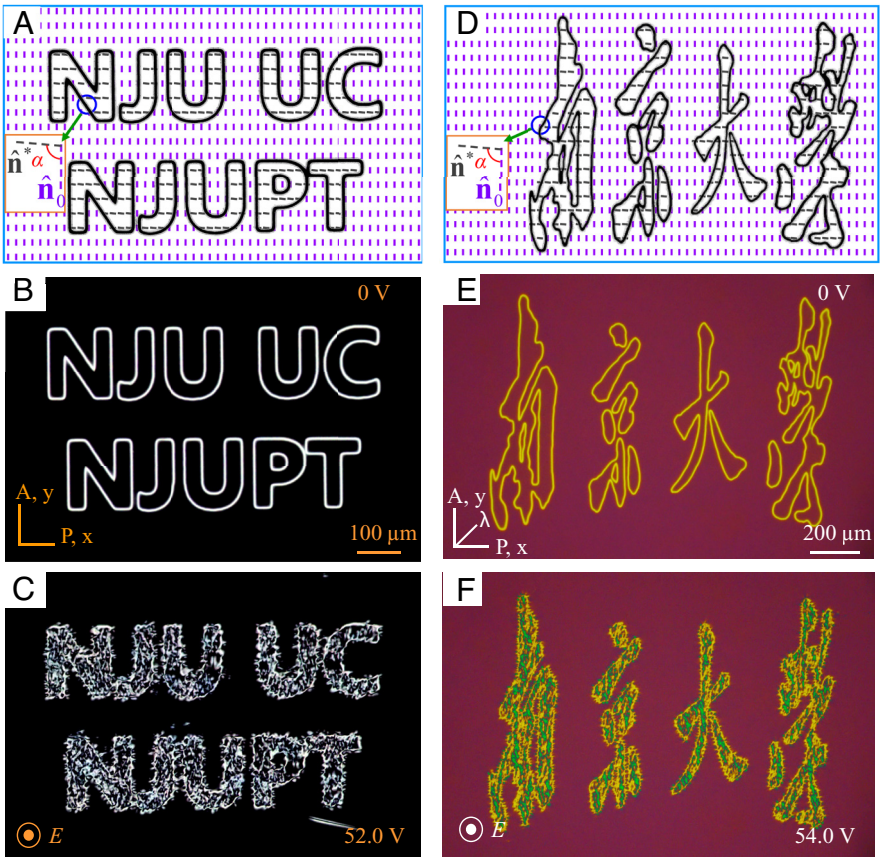

Fig. 6. Steering and patterned localization of directrons. (*A–C*) Director diagram, polarizing optical image, and saturation of directrons for the designed letters NJU, UC, and NJUPT (representing Nanjing University, The University of Chicago, and Nanjing University of Posts and Telecommunications, respectively), without an optical compensator. (*D–F*) Director diagram, polarizing optical image, and saturation of directrons for the designed Chinese characters for Nanjing University (南京大学), with an optical compensator.

showcases the localization of directrons in the form of the letters "NJU, UC, and NJUPT" and the Chinese characters for "Nanjing University" at f = 500 Hz. We illustrate the shapes to provide a clear distinction between different sections (Fig. 6 *A* and *D*). Within the designed patterns, the director $\hat{\mathbf{n}}^*$ forms an angle α = 91° relative to the outer background $\hat{\mathbf{n}}_0$. Our results affirm that using the photopatterning technique with varied exposure sources enables the confinement of directrons within any desired region, as demonstrated (Fig. 6 and Movies S8 and S9).

Discussion

We examined the capabilities of photopatterning, a promising approach for precision in directron creation and manipulation. This method allows us to produce directrons from specific patterns, termed DMGs. DMGs generate solitons proficiently regardless of whether they contain defects. The photopatterned surface influences the directron generation in several ways. First, the elastic distortions caused by surface patterning reduces the electric field threshold for soliton generation (Fig. 2 *B* and *D*). Second, the region where solitons nucleate under relatively low voltage can be manipulated (Fig. 2 *A* and *C*). Third, the anchoring difference between inner and outer patterns promises the localization of solitons (Fig. 6 *C* and *F*). If pattern with weaker anchoring is comparable to the soliton's size, we can control the generation of soliton at fixed location (Figs. 1*C* and 3). Singular defect lines (disclinations) imitate the irregularities reported in previous work (18) and act as the emission sources in the generation of solitons (Fig. 1 *D* and *F* and *SI Appendix*, Fig. S8). Pattern with disclination is more likely to generate solitons than pattern without defect (*SI Appendix*, Fig. S8) and weaker anchoring is a necessary condition for soliton generation at relatively low voltage. By designing and applying specific patterns, we can strategically generate directrons at specific sites, confine them to targeted regions, and guide their travel routes. Our simulations were instrumental in deciphering these effects, mirroring our empirical findings across various electrical settings and DMG variations. The shift in anchoring energy emerged as a defining factor influencing the observed behaviors, highlighting the pivotal role of anchoring in directron dynamics.

It should be clarified that the nucleation of solitons is closely related to the breaking of symmetry in the z-direction. Existing pieces of literature (18–22, 29) have confirmed the following methods for achieving symmetry breaking in experiments: i) surface imperfections, dust particles, and edges of the electrodes; ii) changes in the director field caused by drastic changes in the local electric field, such as the presence of ions; and iii) solitons themselves, as asymmetric structures in the z-direction, which further excite additional solitons. These scenarios may occur at the orientational boundary between two domains and within the bulk of the inner area. As shown in *SI Appendix*, Figs. S9 and S10, our experimental results demonstrate that solitons can emerge from either the orientational boundary between two domains or from the bulk in the inner area. The generation of solitons at lower voltages both internally and at the boundary is due to weak internal anchoring energy, with the mechanism related to flexoelectric polarization. As the voltage increases, hydrodynamic instabilities cause solitons to fill the patterns, resulting in distortions at the

orientational boundary. When the electric field increases above the threshold voltage U_{em}, the driving force induced by the coupling of flexoelectricity and the electric field can overcome the viscous drag force so that solitonic structure is stable, leading to soliton emission (*SI Appendix*, Fig. S11). We demonstrated that the flexoelectricity-driven force points toward the interior of the soliton (29).

We probed the adaptability of the photopatterning technique across a spectrum of factors, including electric field scenarios, pattern dimensions, and geometries. Moreover, we scrutinized and analyzed the differing orientations of director fields within the internal patterns and the external background. Our findings, supported by simulations, indicate that larger DMGs or those with more pronounced orientation differences require lower voltage for directron generation. This is attributed to the consumption of elastic energy in such configurations. In larger DMGs, the impact of orientation difference is reduced, primarily due to the transition area's smaller proportion in the overall pattern. To enhance control over directrons, we introduced an expanded transition area, which improved our ability to guide directron paths, a result further validated by the simulations.

In our work, the inner pattern initially produces the director solitons and is subsequently occupied by hydrodynamic instability patterns (Figs. 2 and 6). The solitons appear at high frequencies (f) above the critical frequency (f_c), corresponding to the dielectric region of LC electrohydrodynamics (19, 20). Besides hydrodynamic instability, in the study of directrons, there are two phenomena related to electrokinetics: one is directron-induced LC-enabled electrophoresis (34), and the other is dynamic solitons that appear at low frequencies ($f < f_c$), corresponding to the conductive regime of LC electrohydrodynamics (19, 20). In experiments, solitons can also nucleate at low f when the parameter ranges correspond to electrokinetic effects (19, 20).

In summary, this research provides valuable insights into the possibilities utilizing photo patterning to achieve facile control over the generation and propagation of directrons. It is envisioned that the techniques and principles established in this work can enable numerous potential applications based on the dynamic regulation of directrons, including information storage, communication, and microcargo transport.

Materials and Methods

Materials. A single-component LC, CCN-47 (Nematel GmbH), possessing negative dielectric and conductive anisotropies (18) ($\Delta\varepsilon = -4.2$, $\Delta\sigma = -1.2 \times 10^{-9}\Omega^{-1}m^{-1}$, at 45 °C and 4 kHz) was employed to generate directrons. This substance exhibits a nematic phase within a temperature range from 29.9 °C to 58.5 °C. Sulfuric azo-dye SD1 (Dai-Nippon Ink and Chemicals, Japan) is the aligning layer to provide photoreorientation under the illumination of linearly polarized UV light.

Sample Fabrication. Glass substrates coated with indium-tin-oxide electrode were cleaned using ultrasonic bath (SERUTEX S-11, Nihon Measure) for 20 min and UV-Ozone bath for 30 min. To achieve the photoresponsive alignment layer, the substrates were coated with solution of 0.35 wt% SD1 in dimethylformamide (Sigma-Aldrich) at 800 rpm for 10 s and 3,000 rpm for 40 s using a spin processor WS-650Mz-23NPPB, Laurell. After heating on the hot stage for 10 min, pairs of substrates were assembled to form cells of thickness $d = 8.0 \pm 0.3$ μm determined by the 8.0 μm-spacer-doped UV glue. The glue underwent the solidification after 2 min of UV irradiation ($\lambda = 405$ nm). The utilization of the linear polarization UV light of wavelength $\lambda = 405$ nm aligns SD1 and enables the uniform background alignment of NLC. We used a digital microdevice-based microlithography system (OPTRON-120, Nanjing Ningcui Optical Technology) to transfer the predesigned patterns onto LC cells. The arbitrary control of the local distribution of directors can be obtained by adopting the photoalignment agent SD1, through a complex exposure process under UV irradiation $\lambda = 365$ nm, which allows for the fabrication of different DMGs.

Generation and Characterization of Directrons. The generation of directrons was achieved by applying sinusoidal AC voltages on the NLC cells using a wave generator (33522B, Keysight Technologies) and a signal amplifier (ATA-2081, Aigtek). A hot stage (LTS120E, Linkam) was used to control the temperature of NLC. All videos and micrographs were recorded in the transmission mode of a polarization optical microscope (50i POL, Nikon) with a camera (DS-Fi3, Nikon).

Numerical Modeling of Solitons. To corroborate our findings and decipher the precise experimental mechanism, we employ simulation techniques referenced in prior studies (35–37), executed in three dimensions. The director field is represented by the traceless, symmetric Q tensor, defined as $Q_{ij}(r,t) = \frac{S(3n_in_j - \delta_{ij})}{2}$, which encapsulates both spatial and temporal variations. Here, S, $n_{i,j}$, and δ_{ij} stand for the degree of uniaxial nematic order, the nematic director field, and Dirac Delta function, respectively.

The system's free energy density, $\mathcal{F}$, can be divided into four components: the Landau–de Gennes thermal energy term f_{LdG}, the elasticity contribution f_{elas}, the dielectric energy contribution f_{diel}, and the flexoelectricity contribution f_{flex}:

$$\mathcal{F} = \int d^2r \left(f_{LdG} + f_{elas} + f_{diel} + f_{flex}\right). \quad [1]$$

To model the temporal evolution of the material, we apply the following equation for dynamic relaxation:

$$\frac{\partial Q_{ij}(r,t)}{\partial t} = -\frac{1}{\gamma_1}\frac{\delta \mathcal{F}}{\delta Q_{ij}(r,t)}, \quad [2]$$

where γ_1 denotes the rotational viscosity.

We need to introduce defects when the solitons are generated from fixed area in simulations. To avoid the infinite energy that appears in the defect, we choose tensorial modeling rather than the vectorial (Frank-Oseen) approach.

Characterization of Birefringence of the NLC. The birefringence Δn of CCN47 is characterized by the transmitted light intensity at $\lambda = 633$ nm. The maximum light intensity after a uniformly aligned cell and a pair of crossed linear polarizers is

$$I_{\perp max} = I_0 \sin^2\left[\frac{\pi \Delta n d}{\lambda}\right]. \quad [3]$$

By fitting $I_{\perp max}$ and the incident light intensity I_0 in different thicknesses of samples, d, the Δn of CCN47 can be determined.

Comparison of Azimuthal Anchoring Energy. To assess the anchoring energy across various photopatterned samples exposed to two distinct UV wavelengths, we estimated the ratio of azimuthal anchoring energies utilizing twist NLC cells, drawing from the method advanced by Collings et al. (38). The twist cells were constructed such that the orientations of SD1 on the top and bottom substrates formed an angle of 90°. After introducing CCN47 into these cells during its isotropic phase, we allowed light of wavelength 633 nm to pass through a configuration of either parallel or perpendicular polarizers with an NLC cell in between. Consequently, we recorded the peak and trough transmitted light intensities as $I_{\parallel}^{iso}$ or $I_{\perp}^{iso}$, respectively. The transmitted light intensity I_i of the NLC in the nematic phase at 55 °C was measured while rotating the sample at different angles at the presence of two crossed polarizers. The normalized transmitted intensity can be calculated by $I = \frac{(I_i - I_{\perp}^{iso})}{I_{\parallel}^{iso}}$. The typical variation in transmission as a function of the angle are shown in *SI Appendix*, Fig. S4. For different cell thicknesses, the maximum I_{max} and minimum I_{min} transmitted light intensities are (38, 39)

$$I_{max} = 1 - \left[\cos\tau\cos\Omega + \left(\frac{1}{\sqrt{1+X^2}}\right)\sin\tau\sin\Omega\right]^2, \quad [4]$$

$$I_{\min} = 1 - \left[\cos\tau\cos\Omega + \left(\frac{1}{\sqrt{1+X^2}}\right)\sin\tau\sin\Omega\right]^2 - \left[\left(\frac{X}{\sqrt{1+X^2}}\right)\sin\tau\right]^2, \quad [5]$$

where Ω is the twist angle of director between the top and the bottom substrates, $X = \frac{\psi}{(2\Omega)}$, $\psi = \left(\frac{2\pi}{\lambda}\right)\Delta n d$, and $\tau = \Omega\sqrt{1+X^2}$. By fitting the normalized transmittance with Eqs. **4** and **5** for samples with various thicknesses, the value of Ω can be determined. Then, the azimuthal anchoring energy is deduced from surface torque equation (39)

$$W\, d\cos\Omega = 2\, k_{22}\, \Omega, \quad [6]$$

where k_{22} is the twist elastic constant of NLCs. Hence, we can obtain the ratio of the azimuthal anchoring energy of patterns irradiated by UV of wavelength 365 nm and 405 nm,

$$\frac{W_{365}}{W_{405}} = \frac{\left(\Omega_{365}\ \cos\Omega_{405}\right)}{\left(\Omega_{405}\cos\Omega_{365}\right)}. \quad [7]$$

The corresponding polar anchoring energy can be calculated from the azimuthal counterpart through the ratio of splay and twist elastic constants of an LC, $\frac{k_{11}}{k_{22}}$ (40).

Data, Materials, and Software Availability. All study data are included in the article and/or supporting information.

ACKNOWLEDGMENTS. The work is supported by the National Key Research and Development Program of China (No. 2022YFA1405000), the National Natural Science Foundation of China (No. 62375141), and the Natural Science Foundation of Jiangsu Province, Major Project (No. BK20212004). N.L.A. and J.J.d.P. acknowledge the support from the Department of Energy, Basic Energy Sciences, Division of Materials Science and Engineering, Biomaterials Program, under grant no. DESC0019762.

Author affiliations: [a]National Laboratory of Solid State Microstructures, College of Engineering and Applied Sciences, and Collaborative Innovation Center of Advanced Microstructures, Nanjing University, Nanjing 210093, China; [b]College of Electronic and Optical Engineering & College of Flexible Electronics (Future Technology), Nanjing University of Posts and Telecommunications, Nanjing 210023, China; [c]Pritzker School of Molecular Engineering, The University of Chicago, Chicago, IL 60637; [d]Smith School of Chemical and Biomolecular Engineering, Cornell University, Ithaca, NY 14853; and [e]Center for Molecular Engineering, Argonne National Laboratory, Lemont, IL 60439

1. T. Dauxois, M. Peyrard, *Physics of Solitons* (Cambridge University Press, Cambridge, 2006).
2. N. J. Zabusky, M. D. Kruskal, Interaction of "solitons" in a collisionless plasma and the recurrence of initial states. *Phys. Rev. Lett.* **15**, 240–243 (1965).
3. P. Heidmann, I. Bah, E. Berti, Imaging topological solitons: The microstructure behind the shadow. *Phys. Rev. D* **107**, 084042 (2023).
4. G. Herink, F. Kurtz, B. Jalali, D. R. Solli, C. Ropers, Real-time spectral interferometry probes the internal dynamics of femtosecond soliton molecules. *Science* **356**, 50–54 (2017).
5. T. Heimburg, A. D. Jackson, On soliton propagation in biomembranes and nerves. *Proc. Natl. Acad. Sci. U.S.A.* **102**, 9790–9795 (2005).
6. T. Ling *et al.*, High-speed interferometric imaging reveals dynamics of neuronal deformation during the action potential. *Proc. Natl. Acad. Sci. U.S.A.* **117**, 10278–10285 (2020).
7. P. Grelu, N. Akhmediev, Dissipative solitons for mode-locked lasers. *Nat. Photon.* **6**, 84–92 (2012).
8. T. J. Kippenberg, A. L. Gaeta, M. Lipson, M. L. Gorodetsky, Dissipative kerr solitons in optical microresonators. *Science* **361**, eaan8083 (2018).
9. M. Peccianti, G. Assanto, Nematicons. *Phys. Rep.* **516**, 147–208 (2012).
10. G. Assanto, *Nematicons: Spatial Optical Solitons in Nematic Liquid Crystals* (Wiley, 2012).
11. J.-S.B. Tai, A. J. Hess, J.-S. Wu, I. I. Smalyukh, Field-controlled dynamics of skyrmions and monopoles. *Sci. Adv.* **10**, eadj9397 (2024).
12. H. R. Sohn, I. I. Smalyukh, Electrically powered motions of toron crystallites in chiral liquid crystals. *Proc. Natl. Acad. Sci. U.S.A.* **117**, 6437–6445 (2020).
13. P. J. Ackerman, J. Van De Lagemaat, I. I. Smalyukh, Self-assembly and electrostriction of arrays and chains of hopfion particles in chiral liquid crystals. *Nat. Commun.* **6**, 6012 (2015).
14. A. Martinez, I. I. Smalyukh, Light-driven dynamic Archimedes spirals and periodic oscillatory patterns of topological solitons in anisotropic soft matter. *Opt. Express* **23**, 4591–4604 (2015).
15. K. B. Migler, R. B. Meyer, Spirals in liquid crystals in a rotating magnetic field. *Phys. D* **71**, 412–420 (1994).
16. H. R. Brand, C. Fradin, P. L. Finn, W. Pesch, P. E. Cladis, Electroconvection in nematic liquid crystals: Comparison between experimental results and the hydrodynamic model. *Phys. Lett. A* **235**, 508–514 (1997).
17. O. D. Lavrentovich, Design of nematic liquid crystals to control microscale dynamics. *Liq. Cryst. Rev.* **8**, 59–129 (2020).
18. B.-X. Li *et al.*, Electrically driven three-dimensional solitary waves as director bullets in nematic liquid crystals. *Nat. Commun.* **9**, 2912 (2018).
19. B.-X. Li, R.-L. Xiao, S. Paladugu, S. V. Shiyanovskii, O. D. Lavrentovich, Three-dimensional solitary waves with electrically tunable direction of propagation in nematics. *Nat. Commun.* **10**, 3749 (2019).
20. S. Aya, F. Araoka, Kinetics of motile solitons in nematic liquid crystals. *Nat. Commun.* **11**, 3248 (2020).
21. S. Das *et al.*, Programming solitons in liquid crystals using surface chemistry. *Langmuir* **38**, 3575–3584 (2022).
22. S. Das *et al.*, Jetting and droplet formation driven by interfacial electrohydrodynamic effects mediated by solitons in liquid crystals. *Phys. Rev. Lett.* **131**, 098101 (2023).
23. Y. Shen, I. Dierking, Dynamic dissipative solitons in nematics with positive anisotropies. *Soft Matter* **16**, 5325–5333 (2020).
24. Y. Shen, I. Dierking, Dynamics of electrically driven solitons in nematic and cholesteric liquid crystals. *Commun. Phys.* **3**, 14 (2020).
25. Y. Shen, I. Dierking, Electrically driven formation and dynamics of swallow-tail solitons in smectic A liquid crystals. *Mater. Adv.* **2**, 4752–4761 (2021).
26. N. Atzin *et al.*, Minimal model of solitons in nematic liquid crystals. *Phys. Rev. Lett.* **131**, 188101 (2023).
27. A. J. Davidson, C. V. Brown, N. J. Mottram, S. Ladak, C. R. Evans, Defect trajectories and domain-wall loop dynamics during two-frequency switching in a bistable azimuthal nematic device. *Phys. Rev. E* **81**, 051712 (2010).
28. N. Sulaiman, D. Marenduzzo, J. M. Yeomans, Lattice boltzmann algorithm to simulate isotropic-nematic emulsions. *Phys. Rev. E* **74**, 041708 (2006).
29. X.-Z. Tang *et al.*, Generation and propagation of flexoelectricity-induced solitons in nematic liquid crystals. *ACS Nano* **18**, 10768–10775 (2024).
30. D. W. Berreman, Solid surface shape and the alignment of an adjacent nematic liquid crystal. *Phys. Rev. Lett.* **28**, 1683 (1972).
31. V. G. Chigrinov, V. M. Kozenkov, H.-S. Kwok, *Photoalignment of Liquid Crystalline Materials: Physics and Applications* (Wiley, 2008).
32. A. Martinez, H. C. Mireles, I. I. Smalyukh, Large-area optoelastic manipulation of colloidal particles in liquid crystals using photoresponsive molecular surface monolayers. *Proc. Natl. Acad. Sci. U.S.A.* **108**, 20891–20896 (2011).
33. B.-Y. Wei *et al.*, Generating switchable and reconfigurable optical vortices via photopatterning of liquid crystals. *Adv. Mater.* **26**, 1590–1595 (2014).
34. B.-X. Li, R.-L. Xiao, S. Paladugu, S. V. Shiyanovskii, O. D. Lavrentovich, Soliton-induced liquid crystal enabled electrophoresis. *Phys. Rev. Res.* **2**, 013178 (2020).
35. P. J. Ackerman, T. Boyle, I. I. Smalyukh, Squirming motion of baby skyrmions in nematic fluids. *Nat. Commun.* **8**, 673 (2017).
36. X.-Z. Tang, J. V. Selinger, Orientation of topological defects in 2D nematic liquid crystals. *Soft Matter* **13**, 5481–5490 (2017).
37. C. Long, J. V. Selinger, Orientation of topological defects in 2D nematic liquid crystals. *Soft Matter* **17**, 10437–10446 (2021).
38. C. K. McGinn, L. I. Laderman, N. Zimmermann, H.-S. Kitzerow, P. J. Collings, Planar anchoring strength and pitch measurements in achiral and chiral chromonic liquid crystals using 90-degree twist cells. *Phys. Rev. E* **88**, 062513 (2013).
39. C.-H. Peng *et al.*, Patterning of lyotropic chromonic liquid crystals by photoalignment with photonic metamasks. *Adv. Mater.* **29**, 1606112 (2017).
40. M. Vilfan, M. Čopič, Azimuthal and zenithal anchoring of nematic liquid crystals. *Phys. Rev. E* **68**, 031704 (2003).